ADVANCED MATERIALS
www.advmat.de

Synergistic Cascade Carrier Extraction via Dual Interfacial Positioning of Ambipolar Black Phosphorene for High-Efficiency Perovskite Solar Cells

Meng Zhang, Meidan Ye, Wenlong Wang, Chunyuan Ma, Shun Wang, Qiliang Liu, Tianquan Lian, Jinsong Huang, and Zhiqun Lin**

2D black phosphorene (BP) carries a stellar set of physical properties such as conveniently tunable bandgap and extremely high ambipolar carrier mobility for optoelectronic devices. Herein, the judicious design and positioning of BP with tailored thickness as dual-functional nanomaterials to concurrently enhance carrier extraction at both electron transport layer/perovskite and perovskite/hole transport layer interfaces for high-efficiency and stable perovskite solar cells is reported. The synergy of favorable band energy alignment and concerted cascade interfacial carrier extraction, rendered by concurrent positioning of BP, delivered a progressively enhanced power conversion efficiency of 19.83% from 16.95% (BP-free). Investigation into interfacial engineering further reveals enhanced light absorption and reduced trap density for improved photovoltaic performance with BP incorporation. This work demonstrates the appealing characteristic of rational implementation of BP as dual-functional transport material for a diversity of optoelectronic devices, including photodetectors, sensors, light-emitting diodes, etc.

Dr. M. Zhang, Dr. M. Ye, Prof. Z. Lin
School of Materials Science and Engineering
Georgia Institute of Technology
Atlanta, GA 30332, USA
E-mail: zhiqun.lin@mse.gatech.edu

Dr. M. Zhang, Prof. W. Wang, Prof. C. Ma
National Engineering Laboratory for Reducing Emissions from Coal Combustion
School of Energy and Power Engineering
Shandong University
Jinan 250061, P. R. China

Prof. S. Wang
College of Chemistry and Materials Engineering
Wenzhou University
Wenzhou 325035, P. R. China

Q. Liu, Prof. T. Lian
Department of Chemistry
Emory University
Atlanta, GA 30322, USA

Prof. J. Huang
Department of Applied Physical Sciences
University of North Carolina
Chapel Hill, NC 27599, USA
E-mail: jhuang@unc.edu

The ORCID identification number(s) for the author(s) of this article can be found under https://doi.org/10.1002/adma.202000999.

DOI: 10.1002/adma.202000999

The past decade has witnessed rapid advances in perovskite-based materials and devices, including perovskite solar cells (PSCs), light-emitting diodes, photodetector, scintillators, etc., due to the largely unique optical and optoelectronic properties of perovskite such as high absorption coefficient, long carrier diffusion length, and low electron–hole recombination rate constant.[1–3] Notably, the organolead halide PSC has reached a certified champion power conversion efficiency (PCE) of 25.2%, yet still distances from the theoretical Schockley–Queisser limit (≈33%).[4] In PSCs, the charge transport layer (electron transport layer [ETL] and hole transport layer [HTL]) are indispensable for yielding best-performance devices due to their ability to effectively separate the electron–hole pairs. However, their unparalleled electronic properties to perovskites greatly hinder the further improvement of cell performance.[5] For example, the most widely used TiO_2 as an ETL and spiro-OMeTAD as a HTL possess the electron and hole mobilities of ≈1 $cm^2\ V^{-1}\ s^{-1}$[6] and ≈10^{-3} $cm^2\ V^{-1}\ s^{-1}$,[7] respectively, which are much lower than that of perovskite absorbers (e.g., 10 $cm^2\ V^{-1}\ s^{-1}$ for $CH_3NH_3PbI_3$[8]). Clearly, the ability to enhance the charge transfer properties of ETL and HTL materials largely represents an important endeavor toward high-efficiency PSCs.

Recently, black phosphorene (BP), a monolayer or several-layer thick black phosphorus, has emerged as an exciting 2D nanomaterial for use in electronics and optoelectronics owing to their outstanding tunable optoelectronic properties and high carrier mobility.[9] In the latter context, BP is an intriguing ambipolar semiconductor with extremely high electron (μ_e) and hole (μ_h) mobilities. Theoretical calculations have predicted an anisotropic effective μ_e of BP (i.e., a lateral, in-plane μ_{e_i} of 1100–1140 $cm^2\ V^{-1}\ s^{-1}$ and a vertical, out-of-plane μ_{e_o} of ≈80 $cm^2\ V^{-1}\ s^{-1}$, respectively), and μ_{h_i} and μ_{h_o} of BP are 640–700 $cm^2\ V^{-1}\ s^{-1}$ and 10000–26000 $cm^2\ V^{-1}\ s^{-1}$, respectively.[9,10] Such extraordinary charge carrier mobilities of BP over conventionally employed TiO_2 and spiro-OMeTAD are advantageous for the separation and transport of electrons and holes for optoelectronic applications. Notably, to capitalize effectively on BP for photovoltaics, it is of key importance in

matching its energy level (i.e., favorable energy level alignment) to that of other constituents in the device. Nonetheless, BP has a thickness-dependent, tunable direct bandgap (i.e., from ≈0.3 eV in bulk to ≈2.0 eV in monolayer, accompanied by a concurrent splitting of the conduction and valence bands).[10,11] In addition, the electronic structure of BP can also be influenced by strain, the rotation angle between the BP nanosheets, and external electric field applied,[12,13] thereby providing expanded opportunity for more precise tuning of its electronic structure. More importantly, the conduction and valence bands of BP nanosheets are highly tunable via controlling their thickness, typically a few layers, thus rendering the capability of energy level matching with the most commonly used constituents in various solar cells, including PSCs.[11] We note that, in sharp contrast to copious work on conventional HTLs and ETLs for PSCs, the study on exploiting BP solely at either HTL/perovskite[14,15] or ETL/perovskite,[16,17] interfaces for improving performance of PSCs has been comparatively few and limited in scope. Surprisingly, the simultaneous implementation of BP with proper thicknesses at the respective interface in PSCs noted above may impart synchronic enhancement of charge transfer and collection at both HTL/perovskite and ETL/perovskite interfaces, thus significantly increasing the PCE of the resulting PSCs. This, however, has yet to be explored.

Herein, we report, for the first time, the rational positioning of ambipolar BP nanosheets as a dual-functional transport material to impart rapid and concurrent two interfacial carrier extractions in PSCs (i.e., placing ≈3- to 4-layer-thick BP at the ETL/perovskite interface for electron transfer and depositing ≈1-layer-thick BP at the perovskite/HTL interface for hole transfer). The mixed-cation and mixed-halide perovskite of $Cs_{0.05}MA_{0.16}FA_{0.79}Pb(I_{0.83}Br_{0.17})_3$ is chosen as the light absorber. The key to favorable carrier extraction lies in the control over the BP nanosheet thickness to confer suitable energy bands, yielding desirable band alignments among the BP, ETL, HTL, and perovskite absorber at the two interfaces. Interestingly, a significantly increased PCE of 19.8% for BP dual-incorporated PSC over either control device (PCE = 16.9%) or device with BP solely placed at either ETL/perovskite (PCE = 18.2%) or perovskite/HTL (PCE = 18.7%) interfaces is achieved as a direct consequence of promoted electron and hole extractions, enhanced light absorption, and reduced trap density at both ETL/perovskite and perovskite/HTL interfaces. Clearly, BP represents an encouraging candidate for tailoring the ETL and HTL characteristics for high-performance PSCs.

The ultrathin BP nanosheets were successfully exfoliated by sonicating the bulk black phosphorous crystals dissolved in IPA under an ice bath (see Experimental Section in Supporting Information). **Figure 1** shows the morphology of as-exfoliated BP nanosheets. The FE-SEM image confirms that the BP nanosheets, prepared by drop-casting on a Si substrate, are randomly yet densely packed, and retain a distinctly layered structure (Figure 1a). They are ultrathin as revealed by TEM (Figure 1b,c). A lattice fringe of 0.34 nm was seen (Figure 1c), which can be ascribed to the (021) plane of orthorhombic phosphorus (ICDD-PDF: No. 76–1963).[14,18] It is important to note that the electron beam could destroy the crystalline BP nanosheets and convert it into amorphous BP during imaging.[19] Due to the ultrathin nature of as-prepared BP nanosheets in our study, it is difficult to obtain high-quality lattice fringe and selected-area electron diffraction patterns. Three typical vibrational peaks at 362.1, 436.6, and 464.5 cm^{-1} were observed in Raman spectroscopy measurement on BP, corresponding to one out-of-plane phonon mode A_g^1 and two in-plane modes B_{2g}, and A_g^2 of BP with a few layers thickness, respectively.[14,19] BP exhibits a strong absorption in the

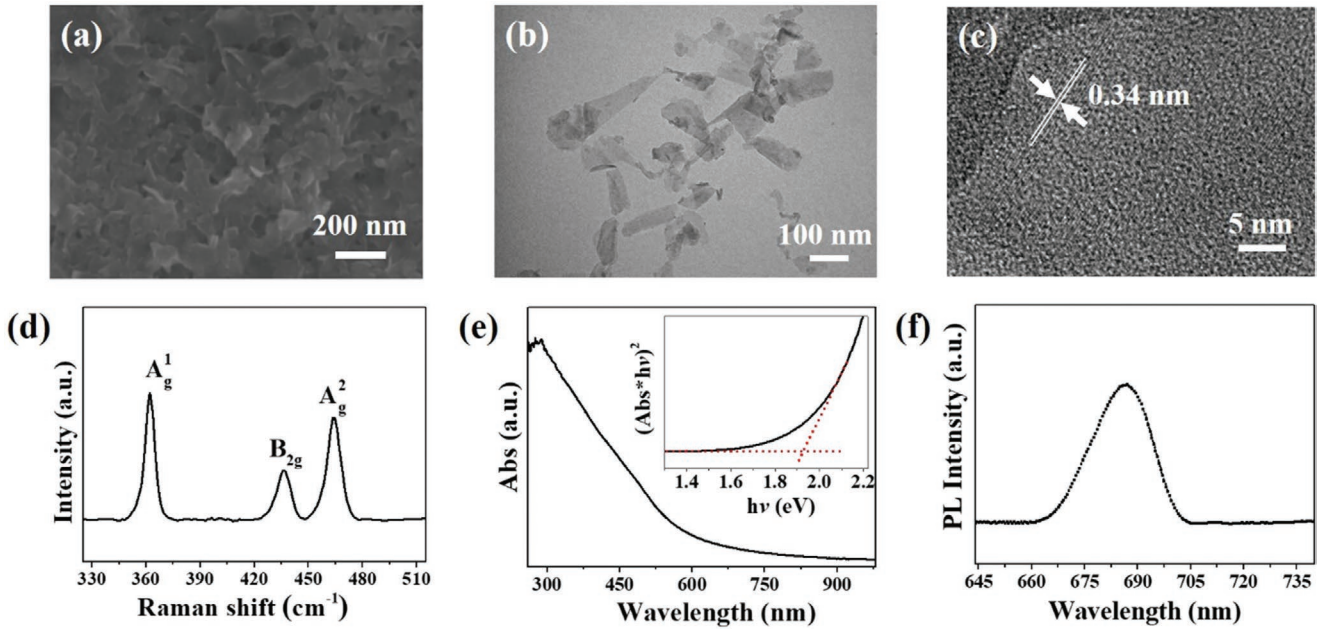

Figure 1. a) Field-emission scanning electron microscopy (FE-SEM) image, b) transmission electron microscopy (TEM) image, c) high-resolution TEM (HRTEM) image, d) Raman spectrum, e) absorption spectrum (inset shows the Tauc plot of the exfoliated BP nanosheets in IPA solution derived from the absorption spectrum), and f) photoluminescence spectrum of the as-exfoliated BP nanosheets in IPA.

UV region and a low absorption in the long visible wavelength region (Figure 1e), consistent with the reports in literatures.[14,20] The bandgap (E_g) of the BP nanosheets in IPA is ≈1.93 eV, calculated from the Tauc plot derived from its absorption spectrum (inset in Figure 1e), which correlates well with a monolayer phosphorene reported in prior works.[10,11] It is notable that BP displays a strongly layer-dependent PL. A strong and broad emission peak at ≈690 nm corresponds to an optical bandgap of ≈1.8 eV (Figure 1f), which is also in accordance with that of a monolayered BP reported.[9] Taken together, the absorption and PL spectra suggest that the exfoliated BP nanosheets exist primarily as a monolayer-thick nanosheets in its IPA suspension.

In order to better reveal the electron and hole extraction ability of BP in PSCs, prior to concurrent positioning at both interfaces for synergistic carrier extraction and transportation in PSCs, the BP nanosheets placed at either ETL/perovskite or perovskite/HTL interface were first investigated separately.

The effect of exfoliated BP on electron extraction was examined in standard n-i-p PSCs using mesoscopic TiO_2 as an ETL (i.e., mesoscopic device). As BP possesses a direct, thickness-dependent bandgap, it is crucial to control the thickness of BP deposited on the TiO_2 layer in order to match the energy level of BP with that of TiO_2 and perovskite absorber. This was enabled by spin-coating the BP IPA suspension on the TiO_2 ETL for different number of times (denoted BP-*n*, *n* refers to the number of spin-coating). With the number of BP coating increased from 1 to 4 (BP-1 to BP-4), the corresponding BP bandgap (deduced from the UV–vis absorption spectra) decreased from 1.54 to 1.12 eV (Figure S2, Supporting Information), confirming the inverse correlation bandgap with its thickness.[10,11] The highest occupied molecular orbital level of the BP film and perovskite absorber were measured using ultraviolet photoelectron spectroscopy (UPS) (**Figure 2**a,b; Figure S1 and Figure S3b, Supporting Information). As summarized in Table S1, Supporting Information, BP-1 and BP-2 have a mismatched conduction band structure with perovskite absorber and TiO_2. In contrast, BP-3 and BP-4 form a cascade conduction band structure with perovskite absorber, which is favorable for efficient electron extraction and thus suppresses the back recombination of electrons with holes near the cathode. Accordingly, the average device efficiency decreased gradually from PCE = 16.2 ± 0.33% to 13.9 ± 0.50% (Figures S4 and S5 and Table S2, Supporting Information) as BP-*n* increased from 0 to 2, while the average PCE increased to 17.3 ± 0.38% and 17.1 ± 0.39% for BP-3 and BP-4, respectively. The highest photovoltaic parameters were derived from BP-3 with the champion device exhibiting a J_{SC} of 23.23 mA cm^{-2}, a V_{OC} of 1.10 V, and an FF of 70.66%, leading to the highest PCE of 18.15% (Figure S4b, Supporting Information). The efficient electron extraction by BP-3 in planar devices were also carried out in parallel, details are shown in Figures S6 and S7 and Table S3, Supporting Information. We note that all PSCs discussed below are mesoscopic devices.

Despite no obvious difference was found in the cross-sectional SEM images of the BP-incorporated devices (Figure S8, Supporting Information), the EDS mapping of phosphorus on BP-*n*-coated (n = 1–4) mesoporous TiO_2 film substantiated the existence of uniformly distributed BP on TiO_2 (insets in Figure 2c, n = 3 and Figure S9, Supporting Information, n = 1, 2, 4). A linear relationship between the BP film thickness and the number of spin-coating was observed with profilometer measurement (Figure S10, Supporting Information). The thickness of BP-3 film is ≈2.3 nm, ≈3 to 4-layer thick.[21,22] The interfacial incorporation of BP-3 did not affect the structure and phase composition of as-prepared perovskite films, as evidenced by powder X-ray diffraction (Figure S11, Supporting Information). However, a larger perovskite grain size distribution was seen for that grown on BP-3-coated mesoporous TiO_2 layer (336 ± 125 nm; Figure 2d; Figures S12d and S13, Supporting Information) compared to that of the pristine mesoscopic counterpart (313 ± 92 nm; Figure S12c, Supporting Information), signifying reduced grain boundary and thus suppressed charge recombination for BP-incorporated devices.[23] The improved perovskite film quality can be ascribed to the BP-assisted perovskite growth. BP was believed to function as heterogeneous nucleation centers during the perovskite crystallization.[14,24,25] Thus, the incorporation of BP on the TiO_2 layer reduced the nuclei density and led to the formation of larger grain size.

No obvious difference was observed in the optical transmission spectra of TiO_2 ETL before and after the BP-3 coating (Figure 2e) due to the thin thickness nature of BP film. However, a notable absorption enhancement was seen in the entire visible wavelength range for the BP-3-incorporated perovskite film (Figure S14b, Supporting Information), which would in turn contribute to the enhanced J_{SC}. The improved light absorption may probably due to the interfacial interaction, that is, the formation of van der Waals heterostructure between 2D BP nanosheets and perovskite, in which charge redistribution at the interface facilitated electron–hole pair separations, thus lead to the enhanced optical properties.[26–28] The enhanced photoluminescence (PL) intensity quenching of the perovskite film upon BP-3 insertion at the TiO_2 ETL/perovskite interface indicated a progressively enhanced charge extraction (Figure S14b, Supporting Information). As BP demonstrates an extremely high electron mobility of 220 cm^2 V^{-1} s^{-1}[29] and up to 1000 cm^2 V^{-1} s^{-1} for thin BP nanosheets (i.e., a few layers),[10] this would facilitate the charge separation and reduce the charge recombination at the interface. In addition, an improved conductivity of BP-3-coated TiO_2 ETL than the pure TiO_2 ETL, as observed in the linear sweep voltammetry (LSV) curves (Figure 2f), suggested a reduced series resistance in the corresponding devices. The charge trap densities n_t in the devices with and without the BP sandwiched at the TiO_2 ETL/perovskite interface were measured from the electron-only space-charge-limited current (SCLC) devices with an architecture of FTO/c-TiO_2/m-TiO_2/BP-3/perovskite/PCBM/Ag (Figure 2g). The calculation of n_t from the trap-filled limit voltage V_{TFL} is detailed in Supporting Information. Notably, a reduced n_t of 1.00×10^{16} cm^{-3} for the BP-3-incopreated device was observed, compared to the control device in the absence of BP-3 introduction (1.13×10^{16} cm^{-3}), which may be attributed to the reduced grain boundary of perovskite crystals, as corroborated by SEM and AFM characterizations (Figures S12 and S13, Supporting Information).

Taken together, by positioning BP-3 at the TiO_2 ETL/perovskite interface, the PCE improvement was resulted from the high carrier mobility of BP and well-aligned conduction band energy of BP-3 with TiO_2 ETL and perovskite absorber for efficient and cascade electron extraction. In addition, the insertion of BP-3 also enhanced light absorption and rendered the

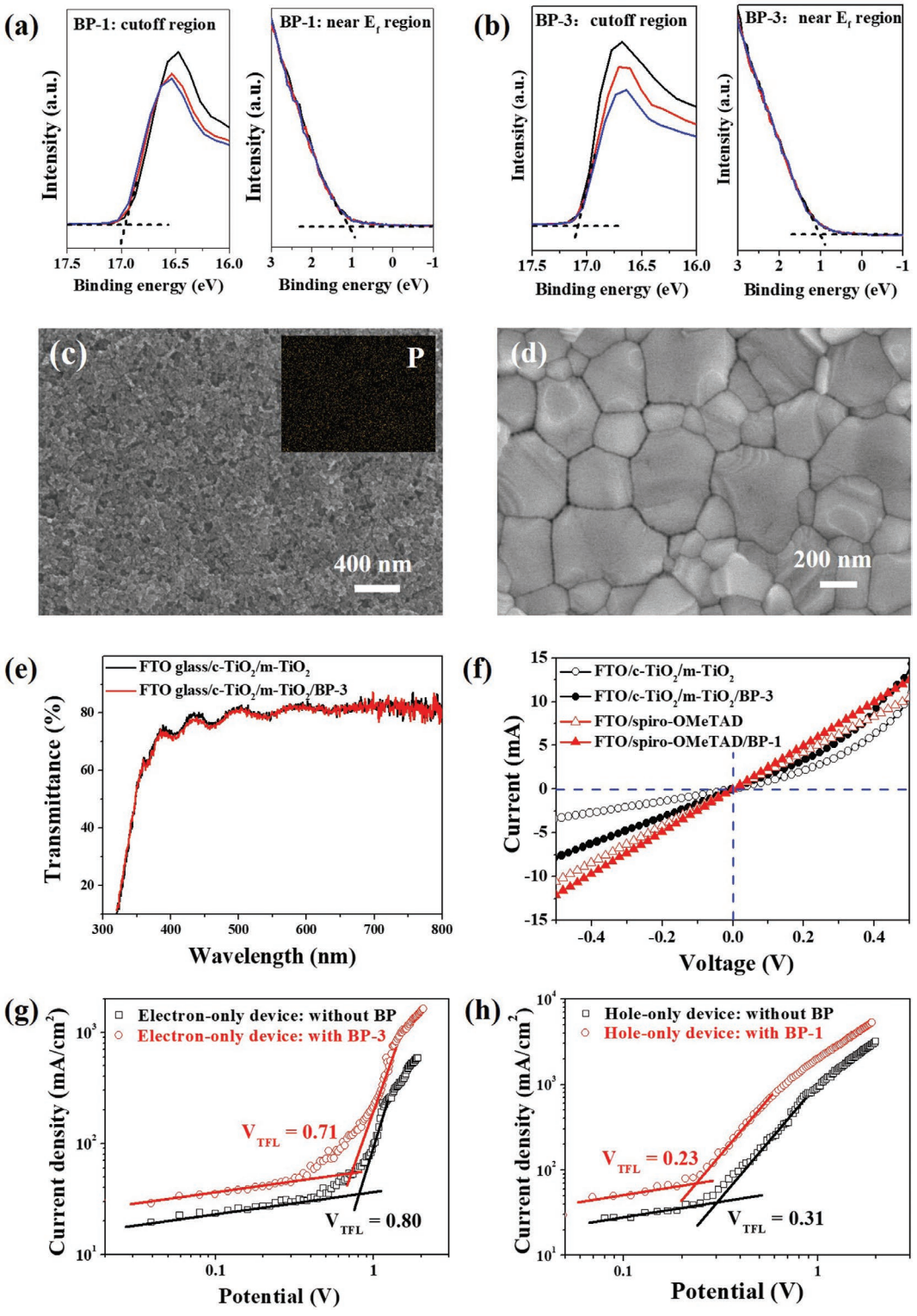

Figure 2. a) The secondary electron cutoff and near Femi energy region of BP-1. b) The secondary electron cutoff and near Femi energy region of BP-3. Notably, BP was coated on silica substrate and the measurements were repeated for three times at different positions as indicated by three different colors. c) SEM image of the BP-3-coated mesoporous TiO_2, where inset shows the corresponding phosphor (P) element mapping. d) SEM image of perovskite absorber on the BP-3-coated mesoporous TiO_2. e) Transmittance spectra of TiO_2 ETL with and without the BP-3 coating. f) Linear sweep voltammetry curves of TiO_2 ETL films with and without the BP-3 deposition and spiro-OMeTAD HTL with and without the BP-1 deposition. g) The *J–V* characteristics of the electron-only space-charge-limited current (SCLC) devices with and without BP-3 positioned at the TiO_2/perovskite interface. h) The *J–V* characteristics of the hole-only SCLC devices with and without BP-1 positioned at the perovskite/spiro-OMeTAD interface.

growth of compact perovskite film with reduced grain boundary. Thus, the charge separation was promoted and charge recombination was suppressed, leading to increased performance of the corresponding device (PCE = 17.3 ± 0.38%) over the pristine device (PCE = 16.2 ± 0.33%) as discussed above.

The exfoliated BP of proper thickness was also found to enable the efficient hole transport when placing it at the perovskite/spiro-OMeTAD HTL interface in PSCs (Table S1, Supporting Information). Based on the UPS results, BP-1 and BP-2 with a cascade energy alignment between perovskite absorber and spiro-OMeTAD HTL were chosen in the study to ensure effective hole transfer from perovskite to HTL.

Similar to the use of BP-3 at the ETL/perovskite interface, the devices with BP-1 and BP-2 sandwiched at the perovskite/HTL interface outperformed the control devices (Figures S15 and S16 and Table S4, Supporting Information), and the highest photovoltaic parameters were seen with BP-1. The champion device with BP-1 insertion exhibited an improved J_{SC} of 23.38 mA cm^{-2}, a V_{OC} of 1.11 V, and an FF of 72.85%, and thus a PCE of 18.86%. Figure S16, Supporting Information, summarizes the statistics of photovoltaic parameters extracted from the *J–V* curves of 24 independent devices. Compared to the control device (PCE = 16.17 ± 0.33%), an average of exceeding PCE of 17.99 ± 0.35% and 17.32 ± 0.33% was observed for the BP-1 and BP-2-incorporated devices, respectively. The improved device performance yielded with BP-1 incorporation over BP-2 can be attributed to its better matched band energy with perovskite absorber and spiro-OMeTAD, which in turn strengthen the hole extraction and block the electron transfer at the perovskite/HTL interface, resulting in a higher PCE.

Likewise, such improved device performance with BP incorporation at the perovskite/HTL interface was derived from the cascade valence band energy alignment for enhanced hole extraction, increased light absorption, and reduced trap states. Notably, the well-aligned band energy in conjunction with the extremely high hole mobility of BP significantly facilitated hole extraction at the interface, as evidenced by the PL spectra (Figure S17b, Supporting Information). At the same time, the BP incorporation also improved the conductivity of HTL, as revealed by the LSV curves of the spiro-OMeTAD film with and without BP-1 coating (Figure 2f), thereby further reducing the corresponding series resistance of the devices. Slightly increased absorbance of the BP-1 incorporated perovskite film, over the entire visible wavelength range (Figure S17b, Supporting Information) is consistent with the increased photocurrent of the devices. Figure 2h compares the *J–V* curves of the hole-only devices (FTO/P3HT/BP-1/perovskite/spiro-OMeTAD/Ag) with and without BP-1 incorporation at the interface, where the V_{TFL} of 0.23 and 0.31 V corresponds to the trap density n_t of 3.25×10^{15} and 4.38×10^{15} cm^{-3}, respectively. This result signifies that the trap state in the perovskite film was effectively passivated by BP at the perovskite/spiro-OMeTAD interface.[14]

As demonstrated above, the exfoliated BP nanosheets could exert the effective electron and hole extraction separately at respective interface in PSC. Thus, we set out to scrutinize if simultaneous introduction of BP at both the ETL/perovskite and perovskite/HTL interfaces (i.e., dual-positioning of BP) yields a synergistically enhanced interfacial carrier extraction for PSC with markedly improved PCE. To this end, the optimized device working conditions for the BP insertion identified at each individual interface were adopted, that is, depositing BP-3 at the ETL/perovskite interface and BP-1 at the perovskite/HTL interface (**Figure 3**a).

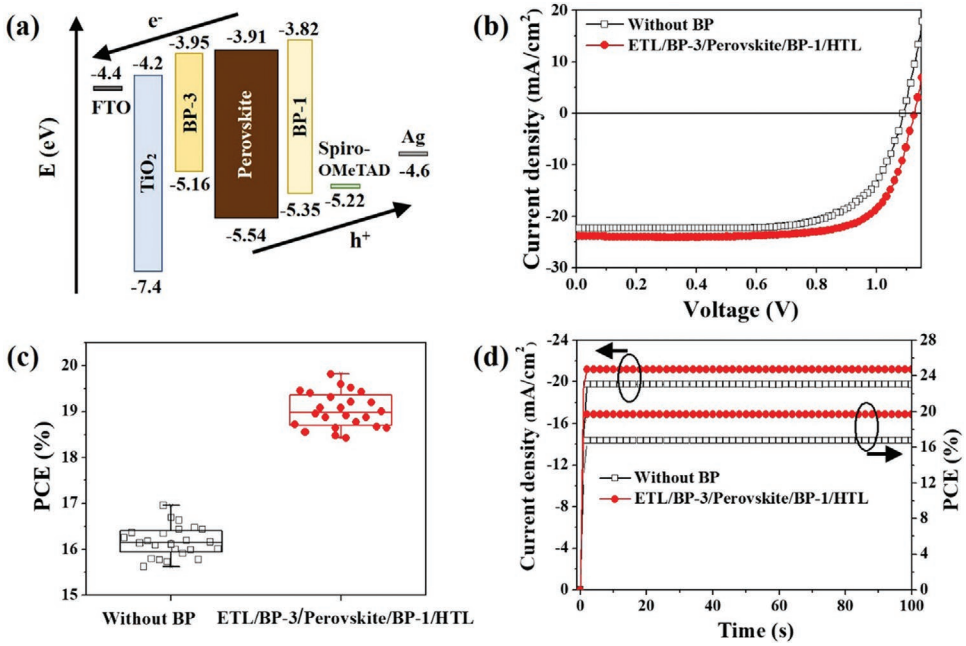

Figure 3. a) Energy level diagram of each constituent in perovskite solar cell with dual-positioning of BP at both interfaces (i.e., BP-3 at the TiO_2 ETL/perovskite interface and BP-1 at the perovskite/spiro-OMeTAD HTL interface). b) *J–V* curves of champion devices with and without BP dual-incorporation. c) Photovoltaic performance statistics for the devices with and without BP dual-insertion. d) Stable J_{SC} and PCE of the devices with and without BP dual-introduction.

Figure 3b,c and Figure S18, Supporting Information, summarize the photovoltaic device performance with and without BP dual-positioned at the both interfaces. The champion device with dual-positioned BP demonstrated a J_{SC} of 23.86 mA cm^{-2}, a V_{OC} of 1.12 V, and an FF of 73.82%, and thus a highest PCE of 19.83%. Table S5, Supporting Information, depicts the photovoltaic performance statistics extracted from the *J*–*V* curves of 24 independent devices, where the average PCE increased from 16.17 ± 0.33% for the control devices to 19.02 ± 0.38% for the BP-dual-incorporated devices. Figure 3d shows the stable output powers of 19.70% and 16.80% with the corresponding steady-state current density of 21.18 and 19.75 mA cm^{-2} for the champion devices with and without the BP dual-incorporation, respectively. The highly stable PCE demonstrated the effectiveness of concurrent interfacial tailoring of carrier extraction by capitalizing on BP of proper thickness at each interface. **Figure 4**a displays the incident photon to current conversion efficiency (IPCE) of the devices with and without BP dual-incorporation. Notably, the BP dual-incorporated device possessed a larger IPCE over the entire spectrum compared to the control device, representing a higher integrated J_{SC} of 22.63 mA cm^{-2} than that of the control device (J_{SC} = 20.29 mA cm^{-2}), which is

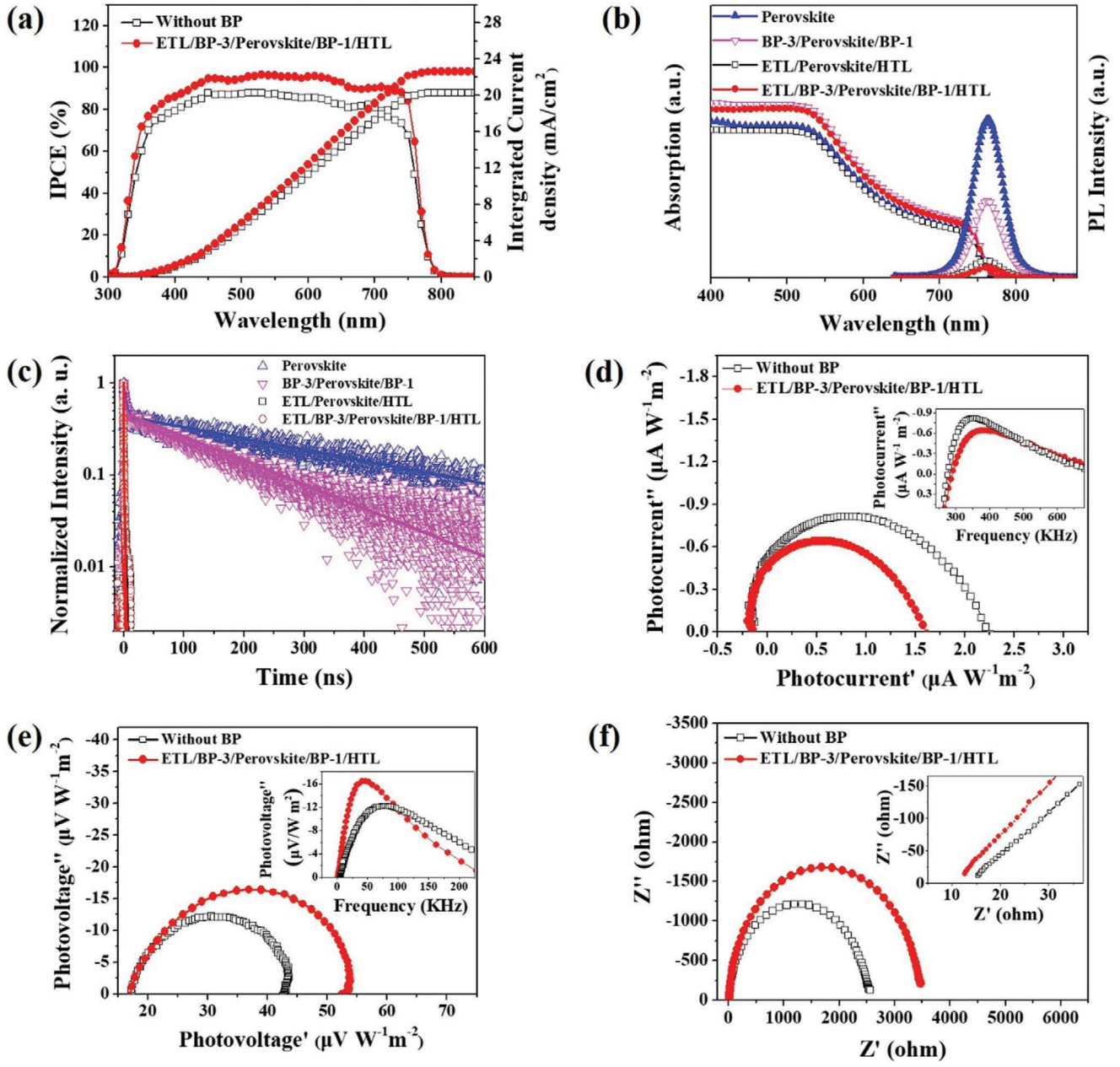

Figure 4. a) IPCE spectra, b) UV–vis and PL spectra, c) time-resolved PL, d) controlled intensity modulated photocurrent spectroscopy (CIMPS) where the inset shows the corresponding Bode plot, e) controlled intensity modulated photovoltage spectroscopy (CIMVS) where the inset shows the corresponding Bode plot, and f) Nyquist plots of electrochemical impedance spectroscopy of perovskite solar cells (PSCs) with and without BP dual-incorporation at both interfaces (i.e., TiO_2/BP-3/perovskite/BP-1/spiro-OMeTAD).

consistent with the J_{SC} enhancement seen in the *J–V* characteristics (Figure 3b). As IPCE = LHE × φ_{inj} × $\eta_{cc,}$ where LHE is the light harvesting efficiency, φ_{inj} is the electron-injection efficiency, and η_{cc} is the charge-collection efficiency,[30] the better device performance with BP dual-insertion is owing to the synergy of intensive light absorption, enhanced charge extraction, facilitated charge transport, and suppressed carrier recombination, as discussed below.

The intense light absorption of the perovskite films upon BP dual-incorporation was confirmed by the UV–vis spectroscopy measurements (Figure 4b; i.e., $A_{BP\text{-}3/Perovskite/BP\text{-}1} > A_{Perovskite}$ and $A_{c\text{-}TiO_2/m\text{-}TiO_2/BP\text{-}3/Perovskite/BP\text{-}1/Spiro\text{-}OMeTAD} > A_{c\text{-}TiO_2/m\text{-}TiO_2/Perovskite/Spiro\text{-}OMeTAD}$), similar to the results shown in Figures S14b and S17b, Supporting Information. Meanwhile, a notable suppression in the PL intensity was found for BP dual-sandwiched perovskite film. The large emission decrease (a 51.50% quenching) signifies the efficient charger transfer from perovskite to BP, further substantiating the dual charge extraction ability of BP as the electron-transport and hole-transport material when in contact with the perovskite absorber. Figure 4c and Figure S19, Supporting Information, compare the time-resolved photoluminescence (TRPL) spectra of the perovskite films confined between different functional layers. The TRPL data was fitted using a bi-exponential decay with a fast decay time τ_1 and a slow decay time τ_2: $A(t) = A_1\exp(-t/\tau_1) + A_2\exp(-t/\tau_2)$, where τ_1 and τ_2 are attributed to the intrinsic band-to-band recombination (radiative recombination) and trap-assisted recombination (non-radiative recombination), respectively.[17,31,32] The average PL decay time τ_{ave} can be estimated using the equation,[17] $\tau_{ave} = (A_1\tau_1^2 + A_2\tau_2^2)/(A_1\tau_1 + A_2\tau_2)$, where A_1 and A_2 are pre-exponential factors. In agreement with the steady-state PL discussed above, the charge-carrier lifetime decreased sharply when functional layers were employed (Table S6, Supporting Information). The τ_{ave} of the pure perovskite film is 348 ± 2 ns, and sharply decreases to 164 ± 1 ns for the BP-3/perovskite/BP-1 film. The τ_{ave} for the TiO_2/perovskite/spiro-OMeTAD is 0.899 ± 0.090 ns, and drops to 0.737 ± 0.083 ns when BP was concurrently incorporated at both interfaces (i.e., TiO_2/BP-3/perovskite/BP-1/spiro-OMeTAD). It is clear that upon the dual-positioning of BP at both interfaces, the well-aligned band energy and high charge extraction ability of BP render more efficient carrier transfer from the perovskite layer to the respective transport layers. The greatly reduced PL decay time is beneficial for suppressing the charge recombination at the ETL/perovskite and perovskite/HTL interfaces.[33] Consequently, the J_{SC} and FF are significantly enhanced (Figure 3b,c; Figure S18, Supporting Information), consistent with the *J–V* and IPCE measurements.

The charge carrier dynamics in the devices with and without BP dual-incorporation were further elucidated by the controlled intensity modulated photocurrent/photovoltage spectroscopy (CIMPS/CIMVS) measurements (Figure 4d,e). The carrier transition time τ_t and carrier lifetime τ_r can be calculated based on the following equations: $\tau_t = 1/(2\pi f_{t,min})$ and $\tau_r = 1/(2\pi f_{r,min})$, where $f_{t,min}$ and $f_{r,min}$ are the characteristic frequencies at the maximum of the CIMPS and CIMVS imaginary component, respectively.[34] A smaller τ_t of 414 ns and a larger τ_r of 3.43 µs for the BP dual-incorporated device than the control device (τ_t = 461 ns and τ_r = 2.17 µs) were found. The shorter τ_t signifies the faster carrier transport. The longer τ_r reflects the suppressed charge recombination, revealing the larger recombination resistance in the devices, which in turn results in the increased V_{OC},[34] as evidenced in the *J–V* characteristics. Moreover, the decreased τ_t and increased τ_r lead to a higher charge collection efficiency η_{cc}, which can be calculated according to $\eta_{cc} = 1 - (\tau_t/\tau_r)$.[35] A higher η_{cc} of 88.10% for the BP dual-incorporated device than that of the control device (η_{cc} = 78.80%) was obtained under an illumination of 1000 W m^{-2} (Table S7, Supporting Information). Thus, it is clear that the BP dual-incorporated devices possess the greater light absorption, enhanced carrier extraction, and larger charge collection efficiency, thereby collectively leading to the higher IPCE (IPCE = LHE × φ_{inj} × η_{cc}[30]) and ultimately PCE.

The improved charge extraction and transport in BP dual-modified devices suggest a larger recombination resistance, which was further corroborated by the electrochemical impedance spectroscopy measurements (Figure 4f). In general, the high-frequency intersection on *x*-axis is ascribed to the serial resistance R_s. The two semicircles observed at high and low frequency region are commonly attributed to interfacial charge transfer resistance R_{ct} and inner recombination resistance R_{rec} together with the corresponding constant phase element CPE, respectively (Figure S20, Supporting Information).[36] A smaller R_S of 12.6 Ω (inset) for the BP dual-incorporated device than that of the control device (R_S = 15.4 Ω) suggests the improved conductivity of the BP-incorporated charge transport layers, correlating well with the LSV results discussed above (Figure 2f). Obviously, R_{rec} dominated in both control device and the BP dual-incorporated device, yet R_{ct} was rather small and comparable (inset; Figure 4f). A larger R_{rec} of 3.5 kΩ for the BP dual-incorporated device than that of the control device (R_{rec} = 2.5 kΩ) suggests a lower charge recombination and more efficient charge dissociation and transport. As a result, the enhanced charge transfer alleviated the interfacial charge loss, thus leading to increased J_{SC} and V_{OC} and in turn improved PCE. The promoted charge transfer and suppressed charge recombination further resulted in a limited hysteresis in the BP dual-incorporated devices (Figure S21, Supporting Information).

The long-term stability is crucial for practical applications of PSCs as the perovskite is highly prone to degradation toward humidity, oxygen, water, UV irradiation, etc. due to its ionic crystal nature.[20,37] In this context, we first evaluated the stability of BP incorporated PSCs (Figure S22, Supporting Information). Substantially unchanged PCE was found for unencapsulated PSCs in dry air, suggesting the solution-processed BP nanosheets in PSCs exhibited relatively good stability. However, the performance of the unencapsulated devices decreased rapidly upon exposure to humid air at a relative humidity of ≈30% (Figure S22a, Supporting Information) mainly due to the perovskite decomposition. In an attempt to increase the moisture stability, PSCs were encapsulated with a hydrophobic 5 µm-thick parylene film via vacuum deposition. Notably, parylene has a high transmittance in the visible light region (Figure S23, Supporting Information). Intriguingly, the PCE of the parylene-protected PSCs retained about 95% of the initial value after 180 days in air (Figure S22b, Supporting Information), manifesting the effectiveness of encasing the PSCs with parylene for prolonged protection from moisture.

In summary, we demonstrated, for the first time, a simple yet robust strategy to enable concerted yet enhanced carrier extraction at both ETL/perovskite and HTL/perovskite interfaces for high-efficiency and stable PSCs by capitalizing on ambipolar BP nanosheets as efficient carrier transport material and simultaneously sandwiching them at the two interfaces. Appealingly, cascade band energy alignments among the BP, perovskite absorber, TiO_2 ETL and spiro-OMeTAD HTL are concurrently attained by tailoring the BP film thickness at the respective interface (i.e., yielding TiO_2 ETL/BP-3/perovskite and perovskite/BP-1/spiro-OMeTAD HTL). As such, the carrier extraction and transfer at the corresponding interface are greatly enhanced due to the extremely high electron and hole mobility of BP, thereby imparting the charge separation and suppressing the charge recombination. The BP-incorporated PSCs also display the improved light absorption, due to the formation of van der Waals heterostructure between BP nanosheets and perovskite, and reduced trap density. Taken together, the synergy of enhanced charge extraction, suppressed carrier recombination, and intense light absorption accounts for the enhanced photovoltaic performance in the BP dual-incorporated device (average PCE = 19.02 ± 0.38%), manifesting a 15% PCE improvement over that of control device without BP (average PCE = 16.17% ± 0.33%). The hydrophobic parylene film encapsulation further increases the device stability against moisture. Clearly, solution-exfoliated BP may stand out as a compelling ambiploar carrier transport nanomaterial for enabling great advances in high-performance optoelectronics via judicious interfacial positioning of BP of tailored thickness.

Supporting Information

Supporting Information is available from the Wiley Online Library or from the author.

Acknowledgements

This work was supported by the NSF (CMMI 1914713, DMR 1903990 and ECCS 1914562). T.L. acknowledges financial support from the NSF (CHE-1709182 and CHE-1726536). J.H. acknowledges financial support from the NSF (DMR 1903981). M.Z. acknowledges financial support from the China Scholarship Council and the China Postdoctoral Science Foundation (2017M612279). The Fundamental Research Funds of Shandong University (2017GN008) and the Opened Fund of the State Key Laboratory of Clean Energy Utilization (ZJUCEU2017010) are also acknowledged.

Conflict of Interest

The authors declare no conflict of interest.

Keywords

ambipolar carrier mobility, band energy alignment, black phosphorene, cascade interfacial carrier extraction, perovskite solar cells

Received: February 12, 2020
Revised: April 4, 2020
Published online:

[1] G. Xing, N. Mathews, S. Sun, S. S. Lim, Y. M. Lam, M. Grätzel, S. Mhaisalkar, T. C. Sum, *Science* **2013**, *342*, 344.
[2] D. B. Mitzi, *Chem. Rev.* **2019**, *119*, 3033.
[3] H. J. Snaith, *J. Phys. Chem. Lett.* **2013**, *4*, 3623.
[4] W. Shockley, H. J. Queisser, *J. Appl. Phys.* **1961**, *32*, 510.
[5] J.-P. Correa-Baena, M. Saliba, T. Buonassisi, M. Grätzel, A. Abate, W. Tress, A. Hagfeldt, *Science* **2017**, *358*, 739.
[6] Q. Zhang, C. S. Dandeneau, X. Zhou, G. Cao, *Adv. Mater.* **2009**, *21*, 4087.
[7] O. Malinkiewicz, A. Yella, Y. H. Lee, G. M. Espallargas, M. Graetzel, M. K. Nazeeruddin, H. J. Bolink, *Nat. Photonics* **2014**, *8*, 128.
[8] C. Wehrenfennig, G. E. Eperon, M. B. Johnston, H. J. Snaith, L. M. Herz, *Adv. Mater.* **2014**, *26*, 1584.
[9] J. Pang, A. Bachmatiuk, Y. Yin, B. Trzebicka, L. Zhao, L. Fu, R. G. Mendes, T. Gemming, Z. Liu, M. H. Rummeli, *Adv. Energy Mater.* **2018**, *8*, 1702093.
[10] A. Carvalho, M. Wang, X. Zhu, A. S. Rodin, H. Su, A. H. C. Neto, *Nat. Rev. Mater.* **2016**, *1*, 16061.
[11] M. Batmunkh, M. Bat-Erdene, J. G. Shapter, *Adv. Mater.* **2016**, *28*, 8586.
[12] J. Kim, S. S. Baik, S. H. Ryu, Y. Sohn, S. Park, B.-G. Park, J. Denlinger, Y. Yi, H. J. Choi, K. S. Kim, *Science* **2015**, *349*, 723.
[13] B. Deng, V. Tran, Y. Xie, H. Jiang, C. Li, Q. Guo, X. Wang, H. Tian, S. J. Koester, H. Wang, *Nat. Commun.* **2017**, *8*, 14474.
[14] W. Chen, K. Li, Y. Wang, X. Feng, Z. Liao, Q. Su, X. Lin, Z. He, *J. Phys. Chem. Lett.* **2017**, *8*, 591.
[15] S. K. Muduli, E. Varrla, S. A. Kulkarni, G. Han, K. Thirumal, O. Lev, S. Mhaisalkar, N. Mathews, *J. Power Sources* **2017**, *371*, 156.
[16] M. Batmunkh, K. Vimalanathan, C. Wu, A. S. Bati, L. Yu, S. A. Tawfik, M. J. Ford, T. J. Macdonald, C. L. Raston, S. Priya, *Small Methods* **2019**, *3*, 1800521.
[17] N. Fu, C. Huang, P. Lin, M. Zhu, T. Li, M. Ye, S. Lin, G. Zhang, J. Du, C. Liu, *J. Mater. Chem. A* **2018**, *6*, 8886.
[18] X. Zhang, H. Xie, Z. Liu, C. Tan, Z. Luo, H. Li, J. Lin, L. Sun, W. Chen, Z. Xu, *Angew. Chem., Int. Ed.* **2015**, *54*, 3653.
[19] Z. Guo, H. Zhang, S. Lu, Z. Wang, S. Tang, J. Shao, Z. Sun, H. Xie, H. Wang, X. F. Yu, *Adv. Funct. Mater.* **2015**, *25*, 6996.
[20] D. Hanlon, C. Backes, E. Doherty, C. S. Cucinotta, N. C. Berner, C. Boland, K. Lee, A. Harvey, P. Lynch, Z. Gholamvand, *Nat. Commun.* **2015**, *6*, 8563.
[21] S. C. Dhanabalan, J. S. Ponraj, Z. Guo, S. Li, Q. Bao, H. Zhang, *Adv. Sci.* **2017**, *4*, 1600305.
[22] Z. Sun, H. Xie, S. Tang, X.-F. Yu, Z. Guo, J. Shao, H. Zhang, H. Huang, H. Wang, P. K. Chu, *Angew. Chem., Int. Ed.* **2015**, *54*, 11526.
[23] M. He, B. Li, X. Cui, B. Jiang, Y. He, Y. Chen, D. O'Neil, P. Szymanski, M. A. Ei-Sayed, J. Huang, *Nat. Commun.* **2017**, *8*, 16045.
[24] Y. Wang, H. Zhang, T. Zhang, W. Shi, M. Kan, J. Chen, Y. Zhao, *Sol. RRL* **2019**, *3*, 1900197.
[25] W. Yang, J. Chen, X. Lian, J. Li, F. Yao, G. Wu, W. Qiu, C. Jin, P. Heremans, H. Chen, *Sol. RRL* **2019**, *3*, 1900132.
[26] B. Liu, M. Long, M.-Q. Cai, J. Yang, *J. Phys. Chem. Lett.* **2018**, *9*, 4822.
[27] Z. Yang, J. Hao, *Small Methods* **2018**, *2*, 1700296.
[28] D. J. Yang, Y. H. Du, Y. Q. Zhao, Z. L. Yu, M. Q. Cai, *Phys. Status Solidi B* **2019**, *256*, 1800540.
[29] R. W. Keyes, *Phys. Rev.* **1953**, *92*, 580.
[30] Z. Yang, C.-Y. Chen, P. Roy, H.-T. Chang, *Chem. Commun.* **2011**, *47*, 9561.
[31] J. F. Liao, W.-Q. Wu, J. X. Zhong, Y. Jiang, L. Wang, D. B. Kuang, *J. Mater. Chem. A* **2019**, *7*, 9025.

[32] J. F. Liao, W.-Q. Wu, Y. Jiang, D. B. Kuang, L. Wang, *Sol. RRL* **2019**, *3*, 1800268.
[33] D. Yang, X. Zhou, R. Yang, Z. Yang, W. Yu, X. Wang, C. Li, S. F. Liu, R. P. Chang, *Energy Environ. Sci.* **2016**, *9*, 3071.
[34] Y. Yang, K. Ri, A. Mei, L. Liu, M. Hu, T. Liu, X. Li, H. Han, *J. Mater. Chem. A* **2015**, *3*, 9103.
[35] X. Meng, X. Cui, M. Rager, S. Zhang, Z. Wang, J. Yu, Y. W. Harn, Z. Kang, B. K. Wagner, Y. Liu, *Nano Energy* **2018**, *52*, 123.
[36] M. He, X. Pang, X. Liu, B. Jiang, Y. He, H. Snaith, Z. Lin, *Angew. Chem., Int. Ed.* **2016**, *55*, 4280.
[37] T. Leijtens, G. E. Eperon, N. K. Noel, S. N. Habisreutinger, A. Petrozza, H. J. Snaith, *Adv. Energy Mater.* **2015**, *5*, 1500963.